JAAS

Journal of Analytical Atomic Spectrometry

www.rsc.org/jaas
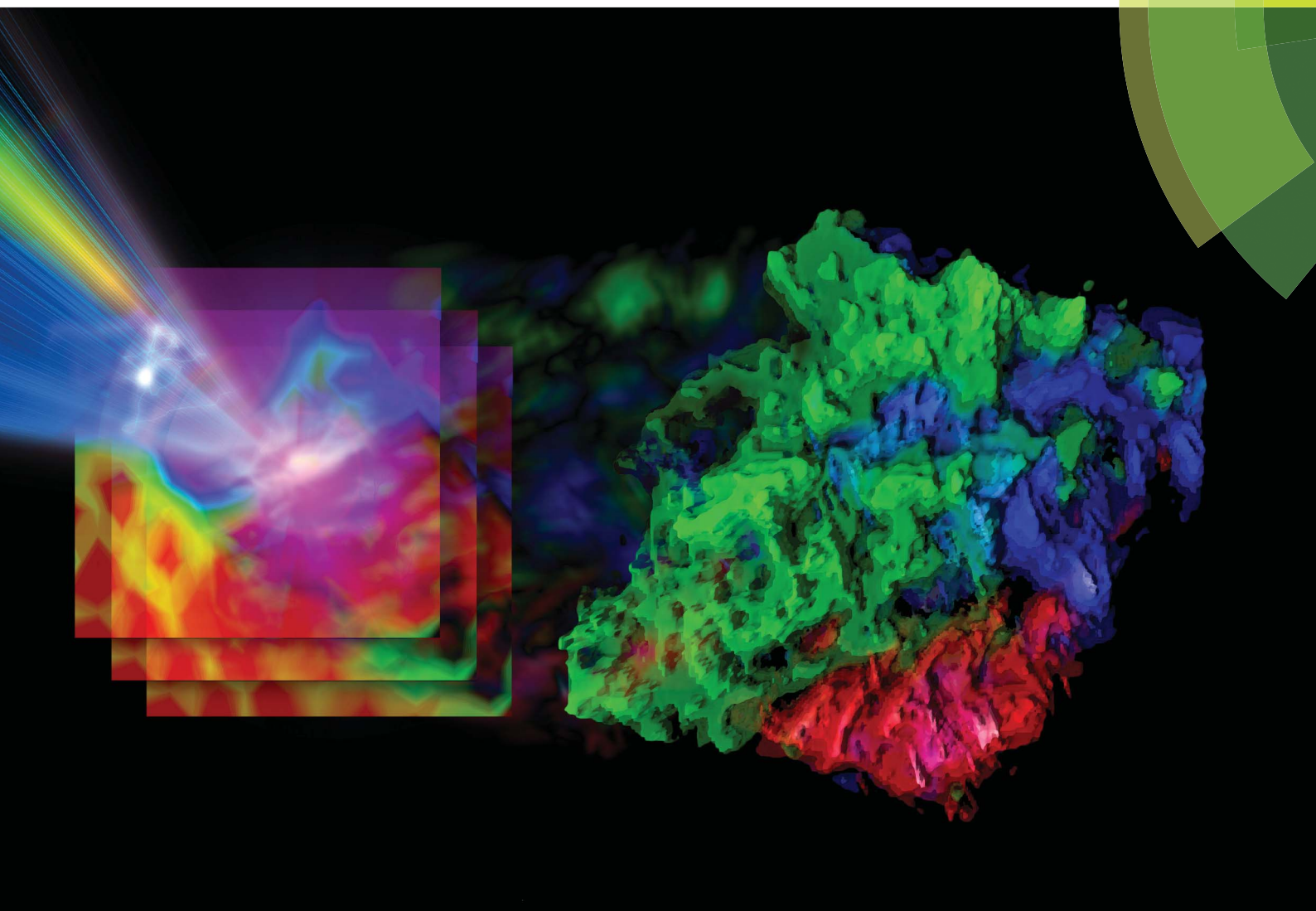
ROYAL SOCIETY
OF CHEMISTRY

TECHNICAL NOTE
Richard E. Russo *et al.*
Simultaneous 3-dimensional elemental imaging with LIBS and LA-ICP-MS

TECHNICAL NOTE

Simultaneous 3-dimensional elemental imaging with LIBS and LA-ICP-MS

Jose R. Chirinos,[a] Dayana D. Oropeza,[a] Jhanis J. Gonzalez,[ab] Huaming Hou,[a]
Mark Morey,[c] Vassilia Zorba[a] and Richard E. Russo*[ab]

Laser Induced Breakdown Spectroscopy (LIBS) and Laser Ablation Inductively Coupled Plasma-Mass Spectrometry (LA-ICP-MS) are used simultaneously for spatially resolved mapping of major and trace elements and isotopes within a *Bastnäsite* rare earth ore sample. The combination of the two techniques provides complementary measurements for elements that are separately unattainable due to low sensitivity and/or strong interferences. Two dimensional (2D) layer-by-layer mapping, 2D cross-sectional imaging and three-dimensional (3D) volume rendering of elements and isotopes in the *Bastnäsite* matrix are presented. These results pave the way for improved 3D elemental imaging through simultaneously acquired LIBS and LA-ICP-MS measurements.

1. Introduction

Laser Ablation Inductively Coupled Plasma-Mass Spectrometry (LA-ICP-MS) is a powerful, direct solid sampling analytical technique for high sensitivity, and precision elemental and isotopic analysis of materials. The process involves a high-power pulsed laser beam directed and focused onto a sample to instantaneously convert a finite volume of the sample into vapor and aerosol constituents (laser ablation) for analysis, followed by transport and excitation of the ablated aerosol to a secondary source (ICP), before entering a mass spectrometer (MS).[1–4] Predominantly used in micro and bulk analysis, LA-ICP-MS has emerged in recent years as a chemical imaging technique where individually sampled spots are correlated to spatially assigned coordinates to produce maps of elements and isotopes. Elemental and isotopic surface (2D) mapping with LA-ICP-MS have been adopted for qualitative and quantitative elemental and isotopic imaging in biochemical applications,[5] ecotoxicology samples,[6] material science,[7] archeology[8] and geochemistry.[9]

Despite the tremendous advances in the sensitivity and resolution of mass analyzers coupled to the ICP source[10] certain elements and isotopes remain largely unmeasurable with LA-ICP-MS. Recurring limiting factors include isobaric and polyatomic interferences, abundance sensitivity and detector saturation which forces masking of specific element masses, and reduced sensitivity due to insufficient ionization of high-ionization potential elements in the argon ICP plasma. These parameters collectively make the detection of elements such as

F, O, H, N, Si, Se, As, Ca, S, with conventional LA-ICP-MS systems very challenging or impossible. As a result, complementary information on these elements is usually provided independently by *ex situ* bulk or surface analysis techniques such as XRF,[11] EDX,[12] fluorescence,[13] Raman,[14] *etc.* prior to LA-ICP-MS sampling. However, cross-correlation between exact sample locations, excitation volumes and resolution (spatial and depth) – which may vary substantially and across different length-scales depending on the *ex situ* analytical technique of choice – can be challenging. Exact control of all these parameters is instrumental in the reliability and consistency of data combined from independent analytical techniques, especially for inhomogeneous samples.

Laser induced breakdown spectroscopy or LIBS is a type of optical emission spectroscopy that provides elemental information by analyzing the spectral content of a plasma resulting from the interaction of a high-power laser pulse with a material.[15–17] The laser sampling process is identical to that used in LA-ICP-MS providing the ability to combine LIBS with LA-ICP-MS for simultaneous chemical analysis from the exact same plasma (sampled mass).

Combining LIBS and LA-ICP-MS is a fairly new concept reported in selected studies limited on surface chemical mapping of materials. Novotný *et al.* studied the elemental distribution of plant tissues and granite samples using 2D maps.[18–21] In these reports the two techniques were used independently by ablating nearby sample locations and with different laser and detection systems therefore no elemental correlation was possible. In contrast, Lackoczy and Ghislain presented 2D maps of magnesium based alloys.[22] The data were obtained simultaneously and due to signal correlation they were able to use Fe mass spectrometry signals to normalize the emission, and reported an improvement on limit of detection of

[a]Lawrence Berkeley National Laboratory, Berkeley, CA 94720, USA. E-mail: rerusso@lbl.gov

[b]Applied Spectra, 46665 Fremont Blvd., Fremont, CA 94538, USA

[c]Special Technologies Laboratory, Santa Barbara, CA 93111, USA

one order of magnitude In this work, we use simultaneous LIBS/LA-ICP-MS to chemically correlate, image and map major and trace elements and isotopes through 2D layer-by-layer and 2D cross-sectional imaging as well as 3D volume reconstruction of the elemental distribution in geological samples. This approach adds the capability of 3D elemental and isotopic mapping of a solid sample by implementing advanced visualization and correlation techniques. A rare earth element (REE)-rich mineral sample of *Bastnäsite*,[23] $(Ce,La)(CO_3)F$, was sectioned with a diamond saw and mapped simultaneously using LIBS and LA-ICP-MS. Complementary data acquired from each technique were merged and overlaid for broad chemical information imaging. The combination of LIBS and LA-ICP-MS opens new capabilities for 2D and 3D visualization of elements and isotopes in material matrices with expanded dynamic range.

2. Experimental methods

A *Bastnäsite* mineral sample was obtained from the MolyCorp Mountain Pass deposit in southeastern California,USA. *Bastnäsite* REE ore was chosen due to its heterogeneity and wide elementary content including most of the lanthanides and some actinides. This sample contains a suite of elements and isotopes with a wide range of bulk concentration, from low parts per million to high percentage levels.[23] A sample with such a variety of elements present provides a good test for applicability range and matrix interference effects. The sample was sectioned with a diamond saw and cleaned with an ultrasonic water bath. The experimental system consisted of a laser ablation system (J200 Applied Spectra, Inc.) coupled to a time-of-flight mass spectrometer from GBC scientific (Fig. 1). The laser ablation system consisted of a frequency quintupled Nd:YAG nanosecond (ns) laser at 213 nm which was focused on the sample surface by a UV microscope objective lens. Spatially resolved 3-D chemical imaging with LIBS and LA-ICP-MS was achieved by scanning the sample across 3-axis (x, y, z) with respect to the

laser beam using high-precision motorized stages (resolution of 100 nm). The crater diameter was 35 μm with an average depth resolution of 3 μm per pulse. The distance between consecutive sampled spots was 50 μm to ensure lack of overlap between sampling locations while maintaining a close distance between neighboring locations. The system was carefully optimized to obtain the highest sensitivity based on a NIST 612 glass sample. Five individual layers were analyzed to create layer-by-layer elemental maps with simultaneous LIBS and LA-ICP-MS. The LIBS system had a collection angle of 45°. Prior to the experiments we verified that side collection did not limit or influence the LIBS signal collection plane and spectral emission imaging for the sampling depth used in this study. Each of the five layers produces a 10 × 10 matrix of data corresponding to an 0.785 × 0.785 mm² area. Following analysis, white-light interferometry (Zygo NewView 6K) was used to determine the laser sampling characteristics.

Laser ablated particles were transported from the ablation chamber to the ICP-Time of Flight-Mass Spectrometer (ICP-TOF-MS) (GBC Scientific Optimass 9000) using helium as a carrier gas, while argon was added to the gas stream as a make-up gas. The ablation delay time between consecutive sampling locations was 10 seconds to avoid the mix of particles in the ICP-MS originating from different ablation events. The plasma optical emission (LIBS) from the laser-sampling location was imaged onto an optical fiber bundle by using a UV fused silica plano-convex lens, with the fiber directly connected to the slit entrance of a spectrometer/ICCD camera system (Acton 2150/Princeton Instruments). The gate of the ICCD camera was triggered by the ns-laser and the relative delay was controlled by the ICCD. The experimental conditions are listed in detail in Table 1.

Prior to LIBS/LA-ICP-MS sampling, the morphology of the *Bastnäsite* sample was measured using dark-field optical microscopy (Olympus BX51). The laser ablation process was monitored using a variable optical zoom system coupled to a
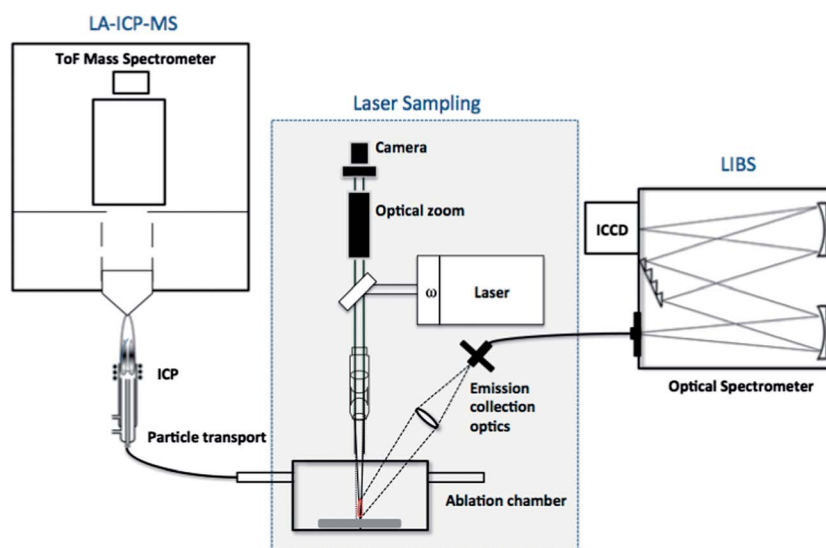

Fig. 1 Experimental setup for simultaneous LIBS and LA–ICP-MS.

Table 1 Experimental conditions

ICP-TOF-MS system (GBC Scientific)	
RF power	1200 W
Plasma Ar flow rate	12.0 L min^{-1}
Auxiliary Ar flow rate	0.60 L min^{-1}
Acquisition parameters	
Acquisition time	200 ms
Acquisition rate	29.41 kHz
Total spectra per reading	5882
Laser ablation/translation stage system	
Wavelength	213 nm
Pulse length	5 ns
Repetition rate	1 Hz
Energy per pulse	6 mJ
Spot size	35 μm
Number of laser passes	5
Number of locations/pass	225
Total sampled area	0.785 × 0.785 mm^2
Optical spectrometer system (Czerny Turner)	
Grating	2400 grooves per mm
Center wavelength	310 nm
Gate width	3.0 μs
Gate delay	800 ns
Carrier(He)/make-up (Ar) flow rate	0.90/0.90 L min^{-1}

CCD camera. Following data acquisition the LIBS and LA-ICP-MS signals were integrated and reassigned to xyz spatial coordinates to produce layer-by-layer 2D elemental maps.

For 3D imaging, a series of visualization techniques were used including color-coding, voxel definition and density dependent opacity. Voxel, short for volume pixel refers to the smallest distinguishable box-shaped part of a three-dimensional image. Stacks of 2D surface elemental maps were produced for every element of interest and served as volumetric datasets. These datasets are used to add depth to an image (voxelization). In 3D imaging, voxels must further undergo opacity transformation, a procedure that provides voxels different transparency based on their individual values. This transformation exposes interior details of an image that would otherwise be concealed by darker and more opaque outer-layer voxels. These visualization methods were adopted to create overlays of multiple elements in 2D surface, 2D cross-sectional and 3D volume elemental images using imaging data examiner software (Amide).

3. Results and discussion

3.1. Simultaneous 2-D surface mapping with LIBS and LA-ICP-MS

LIBS optical emission acquisition was focused on the spectral window from 284 to 333 nm where some of the strongest Si, Ca and Al lines could be measured (Fig. 2a). Multiple atomic and/or ionic lines of elements found in the same spectral window (Ca II 315.88 and 317.93 nm, Al I 308.21 and 309.27/309.28 nm) were used to cross-verify the distribution of elements. The ICP-TOF-MS allowed detection and analysis of most elements up to mass 240 as shown in Fig. 2b. The LIBS and LA-ICP-TOF-MS spectra
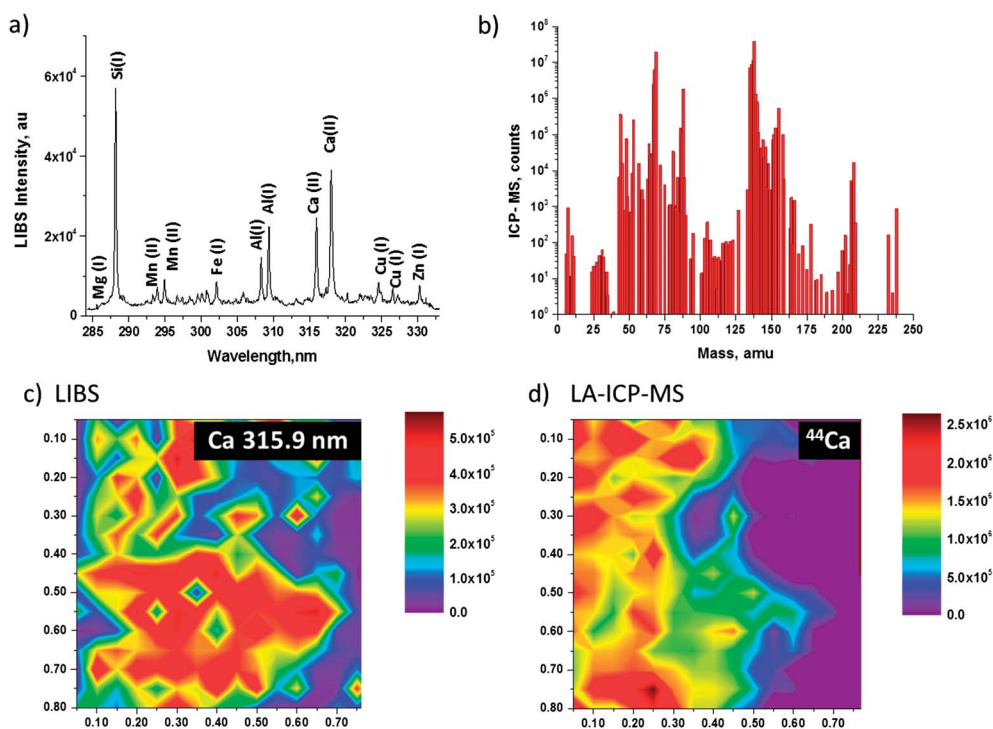

Fig. 2 Representative LIBS (a) and LA-ICP-MS (b) spectra acquired from a single location of the sample. (c and d) Surface (2D) distribution of Ca of the same 0.785 × 0.785 mm^2 area of a *Bastnäsite* rock sample. The Ca maps were obtained simultaneously by (c) LIBS and (d) LA-ICP-MS.

1294 | *J. Anal. At. Spectrom.*, 2014, **29**, 1292–1298

This journal is © The Royal Society of Chemistry 2014

shown in Fig. 2a and b were acquired simultaneously from the same location of the *Bastnäsite* section.

Fig. 2c and d show the 2D contour surface plots of Ca signals for the first 3 μm from the *Bastnäsite* cut surface. The Ca II emission line at 315.89 nm was used to construct the surface plot shown in Fig. 2c. Fig. 2d shows the ^{44}Ca signal from the ICP-TOF-MS map reconstruction. The second highest abundance at ^{44}Ca (2.086%) was chosen because ^{40}Ca, which has the highest natural abundance (96.94%), interferes with ^{40}Ar. On the contrary, LIBS is highly sensitive to Ca. As a result, the sensitivity and signal-to-noise ratios for the ^{44}Ca signal with LA-ICP-MS are inferior to those of LIBS. The differences in the Ca elemental distributions shown in Fig. 2 could be attributed to the difference in the sensitivity of between the two techniques.

Fig. 3 depicts the surface contour maps for elements measured by LIBS in the 284–333 nm spectral range (a)–(c) and LA-ICP-MS (d)–(i) respectively. Maps of Si I (288.1 nm), Ca II (315.9 nm) and Al I (308.2 nm) are shown in (a)–(d). Out of the ~115 masses detected and analyzed with the ICP-TOF-MS we selected to show maps of ^{140}Ce, ^{139}La, ^{146}Nd, ^{208}Pb and ^{55}Mn for brevity. These elements were selected for their wide range of concentration in this sample, from low parts per millions to high percentage levels.[23]

Specific distribution correlations are observed for the selected elements. Correlated groups include Ce, La, Nd and Al, and Mn and Fe. For these elements, high-intensities are measured in the same locations of the rock sample. Elements such as Pb and Ca appear in high concentrations in other locations of the sample and with a varying distribution as compared with the aforementioned groups. The combinations of these element groups are associated with different rock phases.[23]

3.2. Layer-by layer contour plots, cross-sectional imaging and 3-D elemental imaging with LIBS and LA-ICP-MS

Layer-by-layer chemical imaging provides important information on the elemental distribution of materials as a function of depth. This aspect of chemical imaging is increasingly important the more inhomogeneous is the sample. LIBS and LA-ICP-MS both feature layer-by-layer mapping (a combination of surface mapping and depth profiling) that allows imaging the distribution of elements in volume. Layer-by layer contours produced from the same sample at different depths from the surface using LIBS and LA-ICP-MS are shown in Fig. 4. For brevity, only 4 elements are shown – Si I (288.1 nm) and Ca II (315.9 nm) for LIBS and ^{238}U and ^{140}Ce for LA-ICP-MS. These
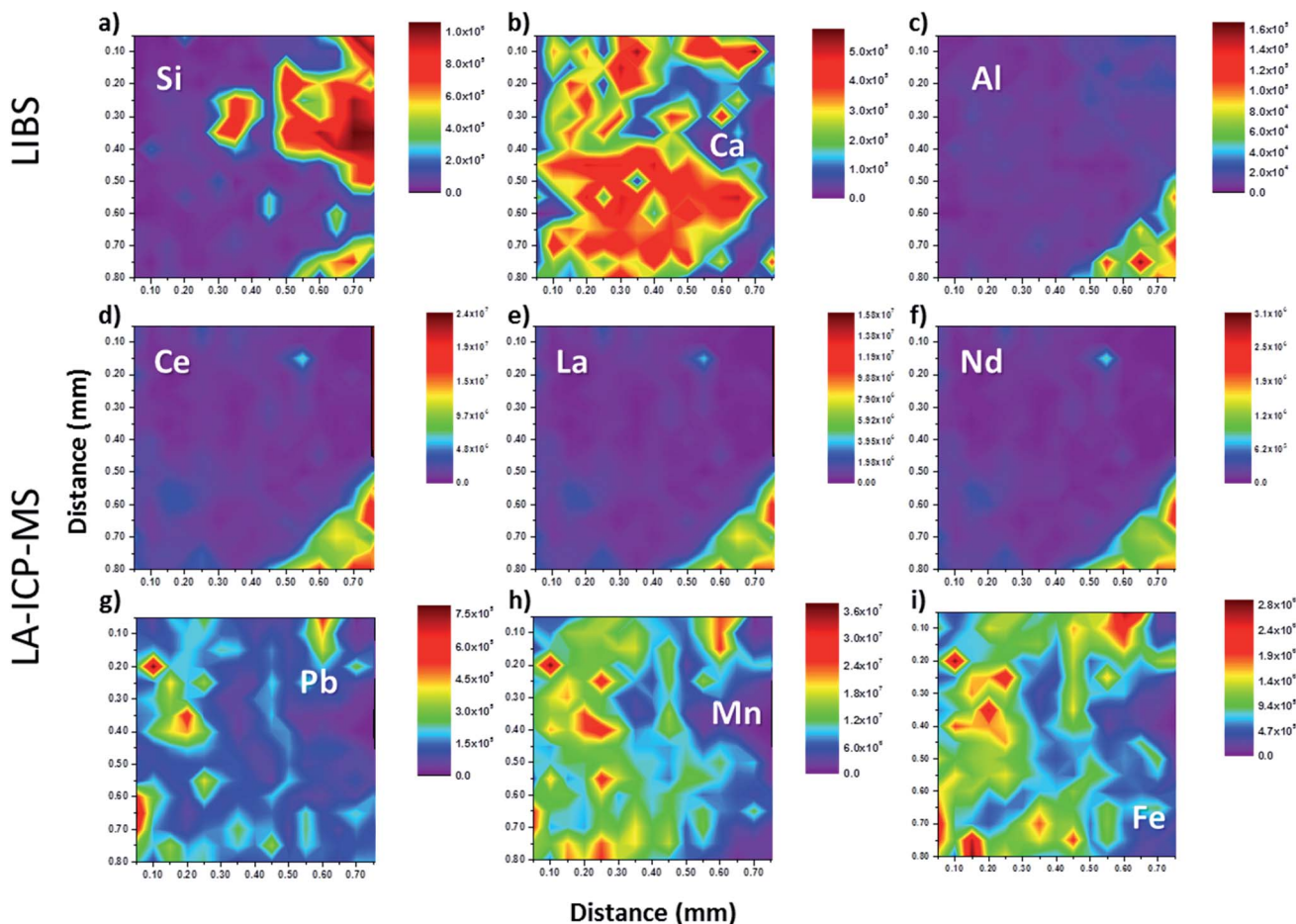

Fig. 3 Simultaneously obtained 2D LIBS surface maps of the *Bastnäsite* rock sample using LIBS and LA-ICP-MS. (a–c) LIBS elemental maps of Si I (288.1 nm), Ca II (315.9 nm) and Al I (308.2 nm). (d–i) LA-ICP-MS maps of ^{140}Ce, ^{139}La, ^{146}Nd, ^{208}Pb, ^{55}Mn and ^{57}Fe.

layers represent the first 15 μm from the sample surface. Small variations were found in the Si distribution as a function of depth. However more pronounced differences were observed in the elemental distribution for Ca, U and Ce as a function of depth.

As the number of layers and data points per element increases, extended visualization capabilities are required to address the dimensionality of the problem. Basic principles of computed tomography were adopted to visualize the distribution of the selected elements in the *Bastnäsite* ore matrix. Reconstruction of 3D distribution of Si, Ca and U involved color-coding, voxel conversion and allocation, as well as integrated intensity (ICP-MS counts or LIBS emission) opacity on each point. Fig. 5a shows a merged overlay of the three elements of interest; U measured by LA-ICP-MS and Ca and Si measured by LIBS. This image represents the third layer analyzed corresponding to 9 um from the sample surface. The red lines across the image correspond to the horizontal and vertical locations along which the cross-sectional 2D images of Fig. 5b are acquired. The merged overlays of LIBS and LA-ICP-MS data in Fig. 5b show the elemental distributions at the selected vertical and horizontal cross sections. Distinct differences in the distribution of each of the selected three elements are observed as a function of depth. This distribution also varies as function on the exact location of the cross section (red lines in Fig. 5a).

Volume reconstruction allows visualization of elements in a material matrix enabling 3D chemical imaging and includes all analytical datasets. A merged overlay of the 3D volume reconstruction is shown in Fig. 5c, with colors corresponding to the following elements: U-red, Ca-green, Si-blue.

3.3. Discussion

Visualization of elements in 3D becomes more elaborate as the number of data points per element increases, a result of improved resolution requirements. Inevitably, resolution, both spatial and depth (or axial), is a key factor in the quantity of data generated and is related to the sample physical characteristics (*e.g.* roughness, porosity, *etc.*). Tightly focused laser beams enable analysis of small sample areas and minimization of the amount of material removed,[24] thereby improving the resolution in LIBS/LA-ICP-MS analysis and in spatially resolved chemical imaging. However, there are cases in which high lateral resolution (less than 10 μm) is not necessary and speed of analysis may be more important, for example in large-area scale analysis.

LIBS and LA-ICP-MS signal acquisition in this study were synchronized to occur from the same location (spot) and plasma. LIBS is an inherently faster technique than LA-ICP-MS; the main reason for this is that LIBS is based on
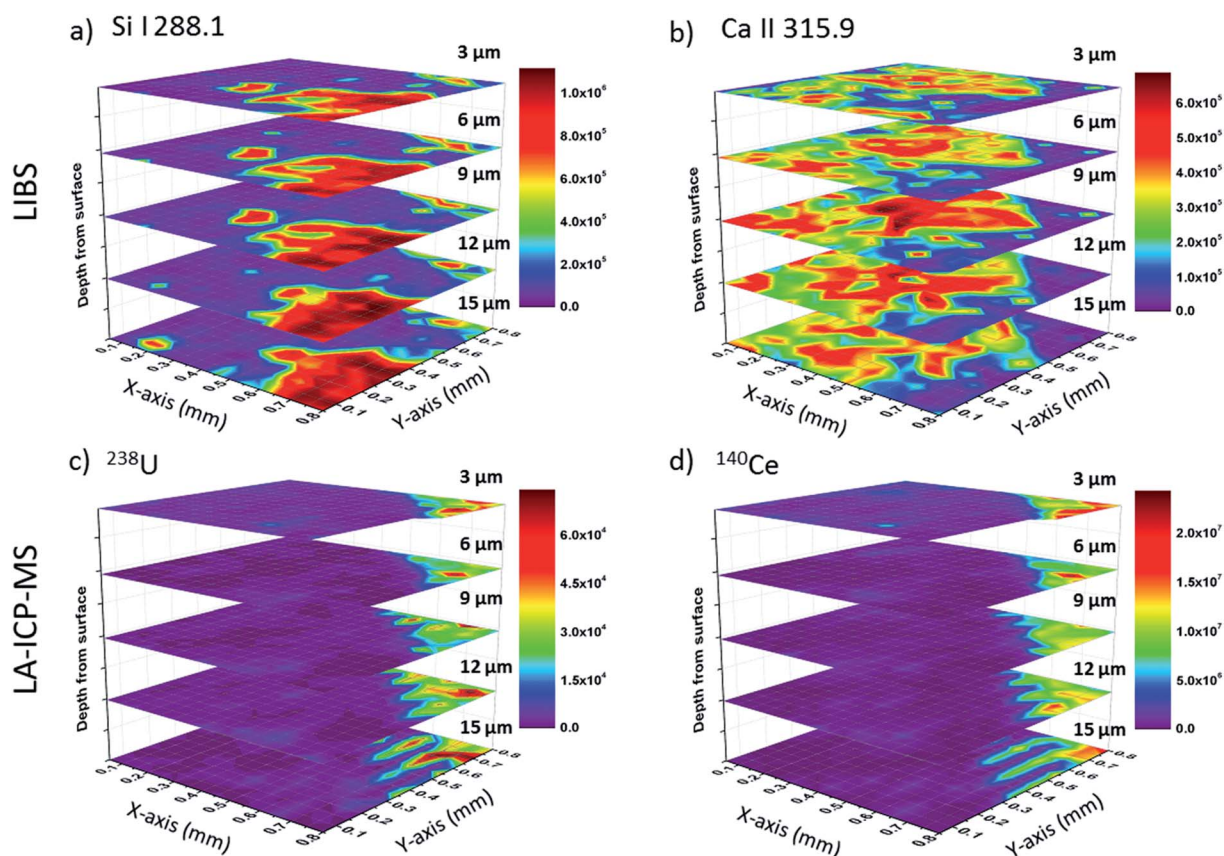

Fig. 4 Layer–by–layer contour elemental maps obtained by simultaneous LIBS/LA-ICP-MS. (a and b) LIBS and (c–d) LA-ICP-MS maps as a function of depth.

1296 | *J. Anal. At. Spectrom.*, 2014, **29**, 1292–1298

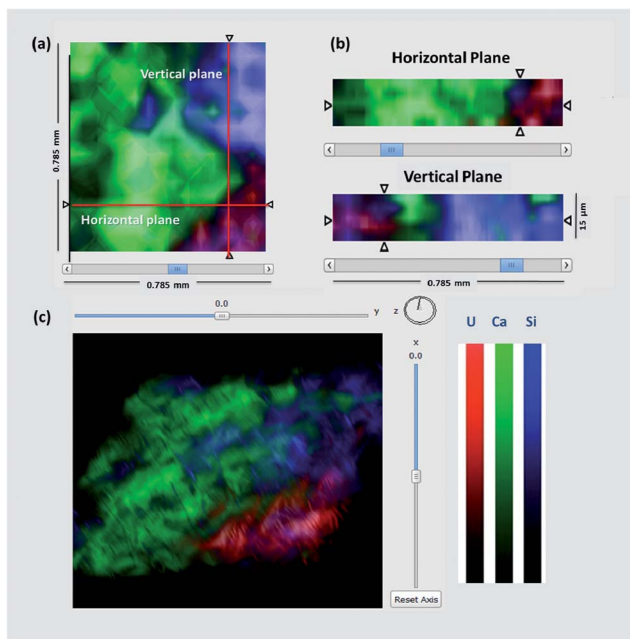This journal is © The Royal Society of Chemistry 2014

Fig. 5 Merged overlay of U, Ca and Si maps. (a) 2D layer imaging, (b) 2D cross-sectional imaging and (c) 3D reconstruction of the elemental distribution in the *Bastnäsite* rock matrix. All data are plotted using a linear color scale where the brightest colors represent the highest intensity. Lateral scale: 0.785×0.785 mm^2, axial scale: 15 μm.

measuring light from the laser induced plasma within microseconds after the laser pulse and does not require the lag time to transport particles from the ablation chamber to the ICP-MS. For ICP-MS, the time for particle evacuation (washout time) from the chamber depends on the total mass ablated, particle size, chamber volume, gas flow rate and sampling pattern. These are the main factors limiting the speed of analysis in spatially resolved elemental and isotopic imaging, and typically restrict the laser repetition rate to 1–5 Hz. However, other factors such as the transport tubing characteristics (*e.g.* length, internal diameter, *etc.*) could delay the particle entrainment into the plasma and influence the overall time of the analysis.

In this study, the spectral range in LIBS acquisition was 50 nm (284–333 nm). However, the use of broadband optical spectrometers *i.e.* Echelle or multichannel Czerny-Turner systems that cover extended spectral ranges (200–900 nm) can enable identification of even more elements of interest in a sample. The use of broadband spectrometers in LIBS will provide a wider dynamic range of complementary information to LA-ICP-MS when the two techniques are used simultaneously. Finally, new developments in the field can be used in conjunction with LIBS/LA-ICP-MS in the next generation of laser-based analytical tools. For example Laser Ablation Molecular Isotopic Spectrometry (LAMIS),[25] a new technology that allows direct isotopic analysis in the laser-induced plasma in real time and at atmospheric pressure, combined with LIBS/LA-ICP-MS could enable significant improvements in sensitivity and precision of laser ablation-based chemical imaging.

4. Conclusion

The combination of LIBS and LA-ICP-MS has the potential of providing expanded elemental coverage from a single sampling event. We demonstrated the simultaneous use of LIBS and LA-ICP-MS as a multifunctional platform for broad chemical information analysis with 2D and 3D imaging capabilities. Computed tomography imaging principles were adopted to visualize multiple elemental and isotopic distributions in a *Bastnäsite* mineral ore matrix.

Acknowledgements

References

1 B. Hattendorf, C. Latkoczy and D. Gunther, *Anal. Chem.*, 2003, **75**(15), 341A–347A.
2 R. E. Russo, X. L. Mao, H. Liu, J. Gonzalez and S. S. Mao, *Talanta*, 2002, **57**, 425–451.
3 E. Russo, X. L. Mao, C. Y. Liu and J. Gonzalez, *J. Anal. At. Spectrom.*, 2004, **19**, 1084–1089.
4 J. Koch and D. Gunther, *Appl. Spectrosc.*, 2011, **65**, 155–162.
5 J. S. Becker, M. Zoriy, A. Matusch, B. Wu, D. Salber, C. Palm and J. S. Becker, *Mass Spectrom. Rev.*, 2010, **29**, 156–175.
6 M. del Rosario Flórez, M. Aramendia and M. Resano, *J. Anal. At. Spectrom.*, 2013, **28**, 1005–1015.
7 J. Elteren, A. Izmer, M. Šala, E. F. Orsega, V. S. Šelih, S. Panighello and F. Vanhaeckeb, *J. Anal. At. Spectrom.*, 2013, **28**, 994–1004.
8 M. Vašinová Galiová, M. Nývltová Fišáková, J. Kynický, L. Prokeš, H. Neff, A. Z. Mason, P. Gadas, J. Košler and V. Kanický, *Talanta*, 2013, **105**, 235–243.
9 J. Woodhead, J. Hergt, S. Meffre, R. R. Large, L. Danyushevsky and S. Gilbert, *Chem. Geol.*, 2009, **262**, 344–354.
10 R. Thomas, *Practical Guide to ICP-MS: A Tutorial for Beginners, Third Edition (Practical Spectroscopy)*, CRC Press, 3rd edn, 2004.
11 Y. Orihashi and T. Hirata, *Geochem. J.*, 2003, **37**, 401–412.
12 H. G. Dill, A. Gerdes and B. Weber, *Mineral. Mag.*, 2007, **71**, 371–387.
13 I. J. Orland, Y. Burstyn, M. Bar-Matthews, R. Kozdon, A. Ayalon, A. Matthews and J. W. Valley, *Chem. Geol.*, 2014, **363**, 322–333.
14 M.-L. C. Sirbescu, E. G. Krukowski, C. Schmidt, R. Thomas, I. M. Samson and R. J. Bodnar, *Chem. Geol.*, 2013, **342**, 138–150.

15 D. W. Hahn and N. Omenetto, *Appl. Spectrosc.*, 2012, **66**, 347–419.

16 D. W. Hahn and N. Omenetto, *Appl. Spectrosc.*, 2010, **64**, 335A–366A.

17 R. E. Russo, T. W. Suen, A. A. Bol'shakov, J. H. Yoo, O. Sorkhabi, X. L. Mao, J. Gonzalez, D. Oropeza and V. Zorba, *J. Anal. At. Spectrom.*, 2011, **26**, 1596–1603.

18 M. Galiová, J. Kaiser, K. Novotný, J. Novotný, T. Vaculovič, M. Liška, R. Malina, K. Stejskal, V. Adam and R. Kizek, *Appl. Phys. A: Mater. Sci. Process.*, 2008, **93**, 917–922.

19 J. Kaiser, M. Galiová, K. Novotný, R. Červenka, L. Reale, J. Novotný, M. Liška, O. Samek, V. Kanický, A. Hrdlička, K. Stejskal, V. Adam and R. Kizek, *Spectrochim. Acta, Part B*, 2009, **64**, 67–73.

20 K. Novotný, J. Kaiser, M. Galiová, V. Konečná, J. Novotný, R. Malina, M. Liška, V. Kanický and V. Otruba, *Spectrochim. Acta, Part B*, 2008, **63**, 1139–1144.

21 M. Galiova, J. Kaiser, K. Novotny, M. Hartl, R. Kizek and P. Babula, *Microsc. Res. Tech.*, 2011, **74**, 845–852.

22 C. Latkoczy and T. Ghislain, *J. Anal. At. Spectrom.*, 2006, **21**, 1152–1160.

23 C. L. Lin, C.-H. Hsieh and J. D. Miller, *Miner. Metall. Process.*, 2013, **30**, 10–17.

24 V. Zorba, X. Mao and R. E. Russo, *Spectrochim. Acta, Part B*, 2011, **66**, 189–192.

25 R. E. Russo, A. A. Bol'shakov, X. Mao, C. P. McKay, D. L. Perry and O. Sorkhabi, *Spectrochim. Acta, Part B*, 2011, **66**, 99–104.